

# Fast Li<sup>+</sup> Transport of Li–Zn Alloy Protective Layer Enabling Excellent Electrochemical Performance of Li Metal Anode

Jinxiang Deng,<sup>[a]</sup> Ying Wang,<sup>\*[b]</sup> Siji Qu,<sup>[a]</sup> Yuchi Liu,<sup>[a]</sup> Wei Zou,<sup>[c]</sup> Fu Zhou,<sup>[c]</sup> Aijun Zhou,<sup>[a]</sup> and Jingze Li<sup>\*[a]</sup>

Li alloy film has been developed as an advanced artificial protection layer on Li metal anode, attributed to its tight contact with Li metal and unique transportation capability of mixed ion/electron. Li<sup>+</sup> diffusion coefficient of the alloy interphase layer is crucial for Li dendrite growth and rate performance. Here, Zn thin film is sputtered on the surface of Li foil, and Li–Zn alloy buffer layer is spontaneously formed via an alloying reaction. In the process of electrochemical cycling, while Li<sup>+</sup> ions are reduced on the interface of the electrolyte

and the anode, the fresh Li atoms rapidly diffuse into the alloy layer via fast ion transport channels of the mixed conductor, resulting in the formation of Li metal free surface. As a consequence, Li–Zn layer protected Li electrode can effectively suppress Li dendrite growth and mitigate the deterioration of Li metal, demonstrating the greatly promoted performance at high current density in both the liquid electrolyte and all solid-state electrolyte systems.

## 1. Introduction

Recently, the electrochemical energy storage has been a hot topic in the world since the electric vehicles are becoming popular year by year. The next generation battery with higher energy density and perfect safety is pursued by both academic and industrial researchers. Li metal is one of the ideal anode materials in terms of its ultrahigh capacity of 3860 mAh g<sup>-1</sup> and the lowest potential of −3.045 V vs. Li/Li<sup>+</sup>.<sup>[1]</sup> Up to now, the commercialization of Li metal anode in the secondary battery has not been realized because Li dendrite growth, low Coulombic efficiency, and infinite volume variation greatly shorten the cycling lifespan and cause safety issues.<sup>[2]</sup>

Many efforts have been devoted to address these problems in the past three decades.<sup>[3]</sup> Three dimensional (3D) architectures have very large surface area, which can provide more active sites to induce Li deposition and significantly reduce the local current density. Recently, porous metal foams,<sup>[4]</sup> 3D carbon structures,<sup>[5]</sup> and nanowire arrays<sup>[6]</sup> have been applied

as current collector or framework of Li composite, leading to the suppressed Li dendrite growth and prolonged cyclic lifetime.<sup>[7]</sup> Unfortunately, the large surface area of these 3D architectures can also render large contact area with the liquid electrolyte. As a result, unexpected side reactions and quick consumption of the liquid electrolyte occur, showing the quickly increased impedance. Furthermore, the 3D architecture occupies a part of the electrode volume and mass, which must decrease more or less the practical capacity of the Li composite anode.<sup>[8]</sup> Alternatively, surface modification is frequently adopted to improve the performance of Li metal anode.<sup>[9]</sup> For example, the additive of the desired inorganic or organic compounds in liquid electrolyte can *in situ* tune the formation process of solid state interphase (SEI) layer showing highly enhanced interfacial stability,<sup>[10]</sup> which leads to the prolonged cyclic lifespan and elevated Coulombic efficiency.<sup>[11]</sup> Certainly, these additives may be consumed up after limited cycles, which cannot in principle guarantee ultra-long lifetime of the cell.<sup>[12]</sup> In this sense, the construction of artificial SEI film on Li metal anode is an promising way.<sup>[13]</sup> Inorganic electrolyte,<sup>[14]</sup> inorganic/organic hybrid electrolyte,<sup>[15]</sup> polymer electrolyte,<sup>[8b, 16]</sup> metal oxide film<sup>[17]</sup> and two-dimensional material<sup>[18]</sup> have been challenged as the coating layer. It should be pointed out that the infinite volume change in the process of Li plating/stripping can lead to the fracture of the coating layer or the peeling of the artificial layer from the Li anode.<sup>[19]</sup> After multiple cycles, Li dendrite growth seems to be unavoidable since the protective effect is gradually weaken.<sup>[20]</sup> Therefore, the advanced coating material and layer structure are still eagerly inspired.

Li alloy protective layers have been intensively studied in light of their unique merits.<sup>[21]</sup> (1) Li alloy layer can be tightly touched with Li metal anode since the protective layer is formed via a facile superficial alloying reaction between the deposited metal and Li anode; (2) Most of the Li alloys have high Li<sup>+</sup> ion diffusion coefficient, which is aided for depressing

[a] J. Deng, S. Qu, Y. Liu, Prof. A. Zhou, Prof. J. Li

School of Materials and Energy

University of Electronic Science and Technology of China

Chengdu 611731, P. R. China

E-mail: lijingze@uestc.edu.cn

[b] Prof. Y. Wang

School of Mechanical and Automotive Engineering

Shanghai University of Engineering Science

333 Longteng Road, Songjiang District, Shanghai 201620, P. R. China

E-mail: wangyingcae@sues.edu.cn

[c] Dr. W. Zou, Dr. F. Zhou

Research and Development Center

Tianqi Lithium Co., Ltd.

Chengdu 610093, P. R. China



Supporting information for this article is available on the WWW under  
<https://doi.org/10.1002/batt.202000125>

An invited contribution to a Special Collection on Lithium Metal Anode Processing and Interface Engineering.

the dendrite growth; (3) The chemical stability of Li alloy is much better than that of pure Li metal, which can effectively passivate the anode surface and hinder the corrosion of organic electrolyte. In general, there are three ways to prepare Li alloy layer. 1) Chemical method: Some metallic cations ( $\text{Al}^{3+}$ ,  $\text{Zn}^{2+}$ ,  $\text{Mg}^{2+}$ ,  $\text{Sn}^{2+}$ ,  $\text{In}^+$ , and so on) are mixed in the liquid electrolyte, then are reduced on the surface of Li metal anode, resulting in the formation of a thin layer of Li alloy promptly.<sup>[22]</sup> Since the chemical environment in the cell is very complicated, the as-obtained alloy layer is generally not in the optimized condition.<sup>[23]</sup> 2) Mechanical method: A Li–In<sup>[24]</sup> or Li–Al<sup>[25]</sup> alloy layer was formed after a conventional In or Al foil sheet was mechanically pressed on the surface of Li metal foil for a while, which can not only improve the chemical stability of the composite electrode against parasitic reactions with the electrolyte, but also enhance  $\text{Li}^+$  ion transport capability across the interfacial layer, leading to excellent electrochemical properties. 3) Physical vapor deposition method: A Si thin layer was sputtered on Li anode, and the subsequent alloying reaction pushed the Si film convert into Li–Si alloy layer, which can uniform Li deposition/dissolution and prolongate the cyclic lifetime significantly.<sup>[21b]</sup> Our group reported a thin Al film coated Li metal via sputtering,<sup>[21d]</sup> where the subsequently formed Li–Al layer passivates the interface and mitigate the deterioration of the anode by suppressing the side reaction effectively. Our further investigation discovered the protective mechanism of the alloy layer.<sup>[26]</sup> Since the alloy is a mixed ion–electron conductor,  $\text{Li}^+$  ions are firstly reduced on the surface of the alloy layer. Then, the fresh Li atoms immediately diffuse into the alloy layer driven by the concentration difference, resulting in the expanding of the layer thickness and the increased concentration of Li atom. The absence of fresh Li metal on the anode surface is the key reason for the improved electrochemical performance. Therefore, the  $\text{Li}^+$  diffusion coefficient of the alloy layer is a critical parameter to determine the mass transfer across the interface between the anode and the electrolyte. As the  $\text{Li}^+$  diffusion coefficient of Li–Al alloy is  $6.0 \times 10^{-10} \text{ cm}^2 \text{s}^{-1}$ , which is slightly superior than  $5.69 \times 10^{-11} \text{ cm}^2 \text{s}^{-1}$  of pure Li metal and lower than that of the intrinsic SEI.<sup>[27]</sup> Thus, the Li–Al alloy protected Li anode can only be operated under low current density.

Li–Zn alloy has high  $\text{Li}^+$  ion diffusion coefficient of  $4.7 \times 10^{-8} \text{ cm}^2 \text{s}^{-1}$ .<sup>[28]</sup> It is reasonable to deduce that Li–Zn alloy protected Li electrode has better kinetic behavior, which is capable to be operated at large current densities with longer cycling lifetime.<sup>[29]</sup> Herein, the symmetric cell with Li–Zn alloy protected Li electrodes can be operated over 500 h and 250 cycles at  $1 \text{ mA/cm}^2$  even in commercial carbonate based electrolyte, which is more than 3 times longer than that of Li–Al alloy coated Li electrode. Furthermore, all solid-state Li battery is the first time to be assembled to evaluate the passivative effect of Li alloy protective layer. The cells with polyethylene oxide (PEO) based polymer electrolyte were operated at  $60^\circ\text{C}$ . Li–Zn alloy coated Li electrode can work more than 900 h at  $0.1 \text{ mA/cm}^2$  and  $0.1 \text{ mAh/cm}^2$ , which is 6 times longer than that of the pristine Li electrode. The reason is

ascribed to Li metal free surface and the enhanced chemical stability of Li–Zn protective layer.

## 2. Results and Discussion

Figure 1a–b illustrates the digital photographs of Li foils before and after sputtering of Zn layer. The pristine Li sheet shows the metallic grey color after mechanically scratching off the native oxide impurity from the surface, and the scratched traces can be clearly observed. After metallic Zn was deposited onto the Li metal sheet via sputtering, the alloying reaction between the Li metal and the Zn film occurred spontaneously, resulting in the formation of Li–Zn alloy coating layer. Meanwhile, the surface color changed from the grey to the golden, suggesting the alloying reaction is successful and the surface of Li foil is uniformly covered with the Li–Zn alloy layer. This result was further confirmed by X-ray diffraction (XRD) characterization, where LiZn crystal phase was identified after the sputtering (Figure S1). Remarkably, the alloy protected Li metal is not very flat at macroscopical scale level, in which many wrinkles appear on the anode surface as shown in Figure 1b. The possible reason is that the alloying reaction leads to huge volume variation, and the film morphology is changed consequently. Therefore, the composite anode needs to be flatten prior to the cell assembling. Notably, the SEM image indicates that the surface seems not very rough at the micrometer scale despite that there are some pits and trenches, which may originate from the pristine Li substrate (Figure 1c and Figure S2). It should be noted that the SEM image of the coated area is very different from that of the uncoated one. The coated area is much brighter than the pristine area, which is attributed to higher secondary electron emission coefficient of Zn element. Furthermore, the cross-sectional SEM image depicts that the existence of the coating layer on the surface, in which the trenches and humps are visualized (Figures 1d–e). Figure 1f is a energy dispersive spectroscopy (EDS) mapping image illustrating the spatial distribution of Zn element in the cross-section. It is clear that the Zn element is concentrated on the top surface, which further confirms the formation of Li–Zn alloy layer. Herein, the

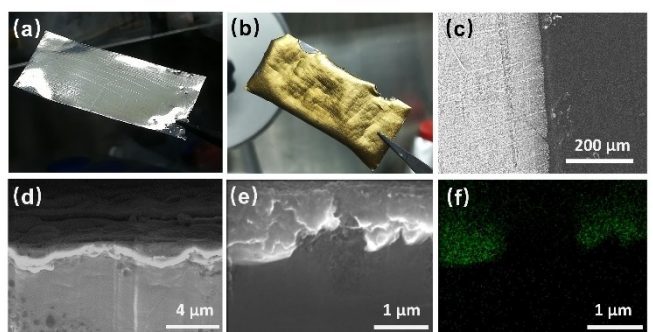
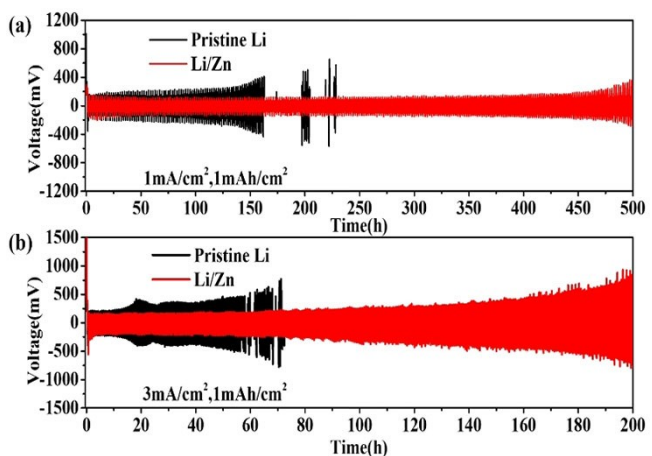


Figure 1. The digital photographs and SEM images of the pristine and Zn coated Li foils. The digital photographs a) before and b) after sputtering of Zn. c) Top-view SEM image of the boundary between the coated and uncoated areas. d–e) The cross-sectional SEM images of the Zn coated Li anode, f) The corresponding EDS mapping image of (e).

thickness of the Li–Zn alloy layer is around 710 nm. As a reference, the Zn film was sputtered onto Si wafer simultaneously. The as-deposited Zn film on Si wafer is porous (Figure S3), which is the aggregation of Zn nanoparticles. The thickness is around 750 nm, which is slightly larger than that of the Li–Zn alloy film. Apparently, the as-deposited Zn atoms react with the underlying Li metal, leading to the formation of Li–Zn alloy layer. As a result, the porous film becomes dense due to the accommodation of Li atoms, resulting in the shrinking of the film thickness and the evolution of the film morphology.

The long-term cycling profiles of the symmetrical cells at  $1 \text{ mA cm}^{-2}$  and  $1 \text{ mAh cm}^{-2}$  were shown in Figure 2a. The cell consisting of the pristine Li foil electrodes is “dead” after 160 h with quickly increased polarization voltage. The poor cycling performance is attributed to serious side reactions between Li metal and the ester based commercial liquid electrolyte, leading to rapid decomposition of organic electrolyte and poor quality of SEI layer. Thus, Li dendrite growth and “dead” Li are easily generated, leading to the loose interface with large impedance. Finally, the cell was suddenly short-circuited with a limited cycling lifetime. As a contrast, the polarization voltage is stably maintained up to 500 h for the coated electrodes, and the maximum cut-off voltage is less than 0.25 V. There is no charging/discharging voltage plateau assigned to the electrochemical de-alloying/alloying reaction (Figure S4), suggesting that the reversible capacity comes from the stripping/ deposition of Li metal. Even the cell was operated under more harsh condition with  $3 \text{ mA cm}^{-2}$ , the modified Li electrode is cycled more than 200 h, and the pristine electrode can only work less than 60 h. Apparently, the Li–Zn buffer layer really passivates the interface, and effectively suppresses the irreversible side reactions in the liquid electrolyte and the generation of side products. The higher  $\text{Li}^+$  ion diffusion coefficient of Li–Zn alloy benefits the rapid transport of  $\text{Li}^+$  through the coating layer, and the Li–Zn alloy coated electrode demonstrates better electrochemical performance under high current density.



**Figure 2.** The electrochemical cycling performances of the pristine Li electrodes and Li–Zn passivated Li electrodes in the configuration of symmetrical cells with commercial ester-based liquid electrolyte at a)  $1 \text{ mA cm}^{-2}$  and  $1 \text{ mAh cm}^{-2}$  and b)  $3 \text{ mA cm}^{-2}$  and  $1 \text{ mAh cm}^{-2}$ .

In order to deeply interpret the protective mechanism, the SEM images of the electrodes after 50 cycles at  $1 \text{ mA cm}^{-2}$  and  $1 \text{ mAh cm}^{-2}$  were recorded, as shown in Figure 3. There are a number of cracks and side reaction products appearing on the surface of the pristine Li electrode. The cross-sectional image indicates that the porous structure extends from the surface into the interior of Li anode. Obviously, the intrinsic SEI layer fails to prevent the Li metal from the corrosion of the electrolyte, leading to the continuous consumption of the electrolyte and Li metal active material cycle by cycle. The similar phenomenon has already been reported by many papers.<sup>[30]</sup> On the contrary, the cycled surface of Li–Zn protected Li metal anode is still very flat and compact, and there is no strong signal of the organic electrolyte decomposition. The corresponding cross-sectional image illustrates that the interior of the Li electrode is still very dense, suggesting the Li–Zn alloy as a buffer layer can physically isolate the bulk Li metal from the liquid electrolyte. Thus, the deposition of Li metal is not greatly affected by the liquid electrolyte. It is also the reason that the thickness of the alloy layer protected electrode keeps constant in the process of electrochemical cycling. It can be concluded that the Li–Zn alloy layer can act as a stable interface and prevent the direct contact between liquid electrolyte and Li anode, and the fast  $\text{Li}^+$  ion diffusion coefficient can aid for Li plating/stripping under high current density, leading to excellent electrochemical performance.

All solid-state Li battery is highly expected to solve the safety problem of Li metal anode. As far as we know, it is the first report to investigate the Li alloy layer protected Li anode in all solid-state battery. Figure 4 shows the cycling performances of the symmetric cells using the composite membrane of PEO, lithium bis(trifluoromethylsulphonyl)imide (LiTFSI), and  $\text{Al}_2\text{O}_3$  nanoparticles as the polymer electrolyte. Since the ionic conductivity of PEO based polymer electrolyte is very poor at room temperature (Figure S5), the cell is operated at  $60^\circ\text{C}$ . The Li stripping/depositing period was fixed as 1 h with a current density of  $0.1 \text{ mA cm}^{-2}$ . The initial polarization voltage of the pristine Li electrode is quickly increased from 35 mV to 180 mV, then the cell suffers from short circuit around 150 h. This result indicates that the interface stability between PEO based polymer electrolyte and pristine Li metal needs to be improved.

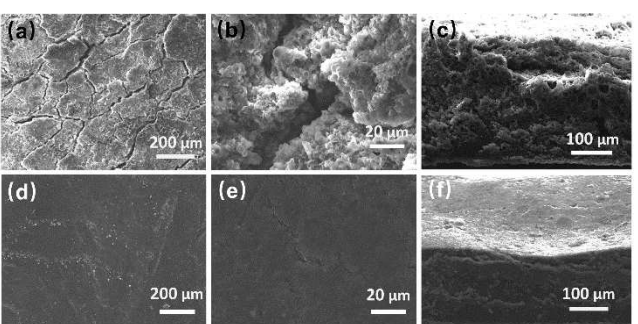


**Figure 3.** The SEM images of the pristine Li electrode (top) and the Li–Zn layer protected Li electrode after 50 cycles at  $1 \text{ mA cm}^{-2}$  and  $1 \text{ mAh cm}^{-2}$ : a–b, d–e) top-view mode and c, f) side-view mode.

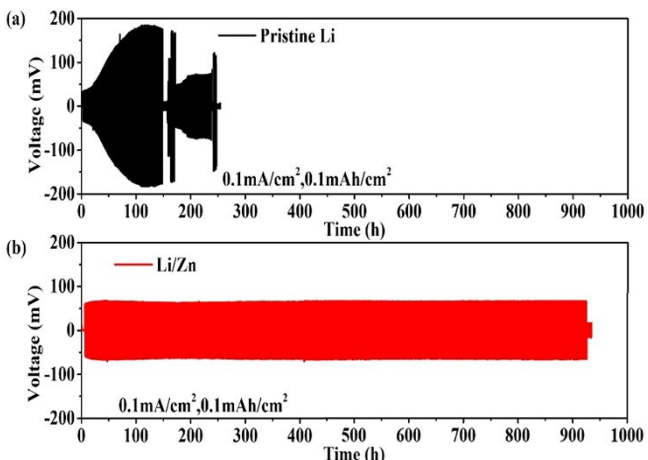


**Figure 4.** The electrochemical performances of the symmetric cells with PEO based polymer electrolyte operated at 60 °C. a) Li pristine electrode and b) Li–Zn layer protected Li electrode.

There are at least two ways to address this problem. One is to modify PEO polymer so as to improve its chemical stability and thermal stability.<sup>[31]</sup> The other is to optimize the surface chemistry of Li metal, which is our methodology in this study.

As for Li–Zn alloy layer coated Li electrode, the initial polarization voltage is 60 mV, which is then increased to 66 mV within few cycles. Remarkably, the initial polarization voltage is higher than that of pristine Li electrode. Since the reduced Li atoms are directly nucleated and plated on the surface of the pristine Li electrode, it is easily to deduce that there is one additional step for the Li–Zn alloy protected Li electrode. The Li<sup>+</sup> ions are reduced on the surface of the alloy layer, then the reduced Li atoms diffuse into the alloy layer and are condensed, which agrees with our previously proposed mechanism.<sup>[26]</sup> Moreover, the cell with the coated electrode is steadily cycled more than 900 cycles, which is 6 times longer than that of the pristine Li.

In order to gain deep insight into the Li stripping/depositing behavior in all solid-state Li battery, the surface morphology of the electrodes was investigated after 20 cycles. As shown in Figure 5a–b, there are a large amount of Li dendrites and mossy Li appearing on the pristine Li electrode, which significantly reduce the actual contact area between the electrolyte and the electrode. Certainly, this situation makes the Li plating and stripping more unevenly. The condition becomes worse and worse, leading to the “dead” of the cell quickly. After cycling, the surface morphology of the alloy passivated surface was completely different from that of the pristine one (Figure 5c–d). The surface is very clean, and there is no aggregation of Li dendrites and dead Li. The white objects might be the residual polymer electrolyte. The alloy protective film is separated into small pieces, which should be induced by the volume difference between the stripping and depositing states.

Figure 6 displays the electrochemical performance of Li<sub>4</sub>Ti<sub>5</sub>O<sub>12</sub> (LTO) full cell with liquid electrolyte and LiFePO<sub>4</sub> (LFP) based all solid-state Li battery. LTO cell is cycled at 2 C (1 C = 175 mAh<sup>-1</sup>). As shown in Figure 5a–b, the cell with the pristine

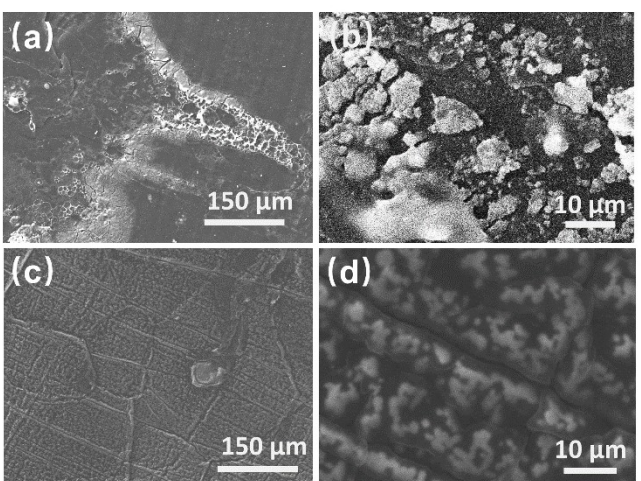


**Figure 5.** SEM images of a, b) pristine Li electrode and c, d) Li–Zn alloy layer protected Li electrode after 20 cycles at 60 °C with PEO based polymer electrolyte.

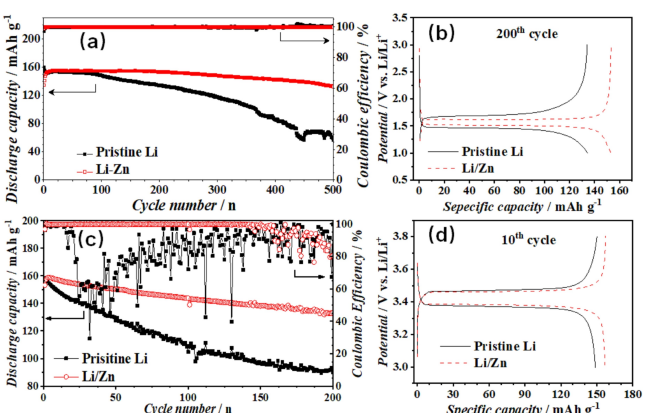


**Figure 6.** Electrochemical performances of the full cells. a) The cycling performance and b) charge/discharge curves at the 200th cycle for LTO/Li cell with liquid electrolyte; c) the cycling performance and d) charge/discharge curves at the 10th cycle for LFP/Li cell with dry polymer electrolyte.

Li anode gives the initial discharge capacity of 159.7 mAh g<sup>-1</sup>, and the capacity retention is 35.6% after 500 cycles. Alternatively, the initial discharge capacity with Zn coated Li anode is 134.6 mAh g<sup>-1</sup>, lower than that with pristine Li anode. After the activation process in the initial few cycles, the capacity is promoted to 155.5 mAh g<sup>-1</sup>. After 500 cycles, the capacity is 132.3 mAh g<sup>-1</sup>, which is equal to the capacity retention rate of 85.1%. Apparently, the cycling performance of the alloy passivated Li anode is much better than that of the pristine one. Furthermore, the polarization voltage is obviously reduced at the 200th cycle, suggesting the alloy coating layer with high Li<sup>+</sup> ion transport can reduce the impedance via the construction of Li metal free interface.

Figure 6c–d depicts the cycling performance of LFP based all solid-state battery. Since LFP electrode utilizes PEO based polymer electrolyte as the binder, the ionic transport capability of the cathode is greatly improved. As a result, the cell can be

cycled at relatively high current rate of 0.5 C ( $0.1 \text{ mA cm}^{-2}$ ). The cell with the pristine Li electrode delivers the initial discharge capacity of  $158.2 \text{ mAh g}^{-1}$ . However, the capacity retention rate is only 61.1% at the 150th cycle, and the average Coulombic efficiency is 81.2%. Moreover, the coulombic efficiency is degraded rapidly and fluctuated even after 21 cycles, indicating there is minor short-circuit caused by the Li dendrite growth. On contrary, the cell with the Zn coated Li anode presents initial discharge capacity of  $153.2 \text{ mAh g}^{-1}$ , and the capacity is  $138.1 \text{ mAh g}^{-1}$  with the retention of 90.1% after 150 cycles. Remarkably, the averaged Coulombic efficiency is as high as 99.7%. Among the reported results, our achievement is one of the best records (Table S1). The dead Li and dendrite growth are suppressed by the modified Li metal anode, offering low electrode polarization and stable interface. Therefore, the modified Li metal anode can demonstrate higher Coulombic efficiency and higher capacity retention. Herein, LFP full cell posses outstanding electrochemical performance even under high current rate.

### 3. Conclusions

Zn layer was sputtered onto the Li anode, then was simultaneously converted into Li–Zn alloy layer via the alloying reaction between Zn layer and Li metal. Since Li–Zn alloy is chemically more stable than that of Li metal, the Li alloy layer can effectively passivate the anode surface, which can significantly suppress dendrite growth and improve the Coulombic efficiency even in the commercial carbonate ester electrolyte. Moreover, the Li–Zn alloy can be operated under high current rate due to its relatively high  $\text{Li}^+$  diffusion coefficient. The modified Li anode can be cycled more than 500 h, with respect to 150 h of the pristine Li anode at  $1 \text{ mA cm}^{-2}$  and  $1 \text{ mAh cm}^{-2}$ . Although the current density is as high as  $3 \text{ mA cm}^{-2}$ , the modified electrode can be cycled over 200 h, and the unmodified Li anode is no more than 60 h. Furthermore, the Li–Zn alloy coated Li electrode behaves well in the PEO-LiTFSI polymer electrolyte based all solid-state battery. LFP full cell can be operated more than 920 h at  $0.1 \text{ mA cm}^2$  (0.5 C). As a reference, the pristine Li anode can be cycled less than 150 h due to a suddenly short circuit induced by Li dendrite. All of these tests confirm that the Zn coated Li electrode can demonstrate excellent electrochemical performance under high current density, where the highly stable interface with fast  $\text{Li}^+$  transport can really aid for uniform Li deposition and stripping under high current rate.

## Experimental Section

### Preparation of the electrode and polymer electrolyte membrane

The alloy protected Li electrode: Li metal foil was from Tianqi Li Co. The purity of Zn target is 99.99%, and the working gas is Ar with 99.999% purity. The optimized sputtering power maintained at 123 W (Figure S6), and the chamber pressure was fixed at 1.0 Pa

with target to substrate distance of 5 cm. In the process of sputtering, the substrate was continuously rotated so as to make the deposited film uniform. The deposition rate was calibrated by depositing Zn film on Si wafer for 10 min, which was around 7.5 nm/min. The Zn film thickness after sputtering of 10 min was around 750 nm.

**Preparation of LTO/LFP cathode:** The active material of LFP powder and electronic conducting additive of Super P were ground with weight ratio of 8:1, then the solution of PEO polymer electrolyte was added as the binder and ionic conducting additive with the weight ratio of LFP:PEO equal to 8:1. The well ground slurry was casted onto the carbon layer coated Al foil, and baked for 5 h at  $60^\circ\text{C}$ . The composite electrode was punched into small discs with the diameter of 10 mm, and was further dried at  $60^\circ\text{C}$  under vacuum for 24 h.

**The solid polymer electrolyte:** PEO and LiTFSI were weighted at the molar ratio of 20:1, which were further mixed with 4 wt.% of  $\text{Al}_2\text{O}_3$  powder. The mixture was stirred in acetonitrile solvent for 24 h. The as-obtained solution was casted onto polytetrafluoroethylene (PTFE) substrate, and the solvent was naturally evaporated in the glovebox. The dry polymer electrolyte membrane was peeled from the substrate, and was punched as the circle sheets.

### The cell assembling

The Li–Li symmetric cells were assembled in Ar filled glovebox with Celgard 2325 separator sheet and a conventional ester based organic electrolyte consisting of  $1 \text{ mol l}^{-1}$   $\text{LiPF}_6$  dissolved in the mixture of ethylene carbonate (EC)/ diethyl carbonate (DEC)/ dimethyl carbonate (DMC) (1:1:1, v/v/v).

**The assembling of all solid-state battery:** The pristine Li foil and Zn coated Li foil were cut into small discs with the diameter of 10 mm. The symmetric cell was composed of two Li metal electrodes and one polymer electrolyte membrane. LFP cell was sandwiched with one LFP electrode, one PEO-LiTFSI membrane and one Li foil electrode. The piled structure was encapsulated with CR2032 coin cell. The LiFePO<sub>4</sub> cell was tested between 3.0–3.8 V vs. Li/ $\text{Li}^+$ , and the current density was 0.5 C (1 C = 170 mA/g).

### The electrochemical test and material characterization

The charge/discharge tests were done with a BTS-5 VOA instrument (Neware Electronic Co. Ltd.) at a temperature of  $25^\circ\text{C}$ . Electrochemical impedance spectroscopy (EIS) curves were recorded with an electrochemical workstation (Parstat 2236) in the frequency range of 1 MHz to 100 mHz with a perturbation amplitude of 10 mV. The LTO composite electrodes were prepared by blending LTO powder, super P and polyvinylidene fluoride (PVDF) at the mass ratio of 8:1:1 in N-methyl-2-pyrrolidone (NMP) solvent. The mixed slurry was casted onto Cu foil and then dried in an oven at  $60^\circ\text{C}$  for 5 h, which were dried in vacuum at  $110^\circ\text{C}$  for 10 h. Finally, the LTO–Li cells were tested in a voltage range of 1.0–3.0 V vs. Li/ $\text{Li}^+$  at a current rate of 2 C (1 C =  $175 \text{ mA g}^{-1}$ ).

The phase structure analysis was performed by XRD with Cu K $\alpha$  irradiation ( $\lambda = 1.5418 \text{ \AA}$ , tube voltage = 40 kV and tube current = 35 mA). The polyimide (PI) film was utilized to protect Li metal from the air.

The top-view and side-view SEM images were recorded with JEOL-JSM-6490LV.

## Acknowledgements

This work is partly supported by the National Natural Science Foundation of China (No. 21673033, 21473022), and the Science and Technology Department of Sichuan Province of China (2019YFH0001).

## Conflict of Interest

The authors declare no conflict of interest.

**Keywords:** Li–Zn alloy • alloy layer • diffusion coefficient • Li metal anode • alloy anode

- [1] M. Armand, J. M. Tarascon, *Nature* **2008**, *451*, 652–657.
- [2] X. Zhang, S. Wang, C. Xue, C. Xin, Y. Lin, Y. Shen, L. Li, C.-W. Nan, *Adv. Mater.* **2019**, *31*, 180682.
- [3] a) J. Wang, P. King, R. Huggins, *Solid State Ionics* **1986**, *20*, 185–189; b) R. A. Huggins, *J. Power Sources* **1999**, *81*–82, 13–19.
- [4] a) H. Zhao, D. Lei, Y.-B. He, Y. Yuan, Q. Yun, B. Ni, W. Lv, B. Li, Q.-H. Yang, F. Kang, J. Lu, *Adv. Energy Mater.* **2018**, *8*, 1800266; b) H. Liu, E. Wang, Q. Zhang, Y. Ren, X. Guo, L. Wang, G. Li, H. Yu, *Energy Storage Mater.* **2019**, *17*, 253–259.
- [5] a) C. Jin, O. Sheng, Y. Lu, J. Luo, H. Yuan, W. Zhang, H. Huang, Y. Gan, Y. Xia, C. Liang, J. Zhang, X. Tao, *Nano Energy* **2018**, *45*, 203–209; b) M. Zhu, B. Li, S. Li, Z. Du, Y. Gong, S. Yang, *Adv. Energy Mater.* **2018**, *8*, 1703505; c) F. Guo, Y. Wang, T. Kang, C. Liu, Y. Shen, W. Lu, X. Wu, L. Chen, *Energy Storage Mater.* **2018**, *15*, 116–123; d) Z. Li, X. Li, L. Zhou, Z. Xiao, S. Zhou, X. Zhang, L. Li, L. Zhi, *Nano Energy* **2018**, *49*, 179–185; e) Z. Sun, S. Jin, H. Jin, Z. Du, Y. Zhu, A. Cao, H. Ji, L. J. Wan, *Adv. Mater.* **2018**, *30*, 1800884; f) C. Zhao, C. Yu, S. Li, W. Guo, Y. Zhao, Q. Dong, X. Lin, Z. Song, X. Tan, C. Wang, M. Zheng, X. Sun, J. Qiu, *Small* **2018**, *14*, 1803310.
- [6] a) W. Zhu, W. Deng, F. Zhao, S. Liang, X. Zhou, Z. Liu, *Energy Storage Mater.* **2019**, *21*, 107–114; b) X.-Y. Yue, W.-W. Wang, Q.-C. Wang, J.-K. Meng, X.-X. Wang, Y. Song, Z.-W. Fu, X.-J. Wu, Y.-N. Zhou, *Energy Storage Mater.* **2018**, *14*, 335–344.
- [7] W. Jia, Z. Wang, J. Li, X. Yu, Y. Wei, Z. Yao, Y. Liu, Y. Wang, A. Zhou, W. Zou, F. Zhou, H. Li, *J. Mater. Chem. A* **2019**, *7*, 22377–22384.
- [8] a) L. Kong, H.-J. Peng, J.-Q. Huang, Q. Zhang, *Nano Res.* **2017**, *10*, 4027–4054; b) N. Goujon, T. V. Huynh, K. j Barlow, R. Kerr, K. Vezzù, V. D. Noto, L. A. O'Dell, J. Chieffari, P. C. Howlett, M. Forsyth, *Batteries* **2019**, *2*, 132–138.
- [9] a) H. Wang, Y. Liu, Y. Li, Y. Cui, *Electrochem. Energy Rev.* **2019**, *2*, 509–517; b) Y. Zhao, M. Amirmaleki, Q. Sun, C. Zhao, A. Codiretti, L. V. Goncharova, C. Wang, K. Adair, X. Li, X. Yang, F. Zhao, R. Li, T. Filleteer, M. Cai, X. Sun, *Matter* **2019**, *1*, 1215–1231.
- [10] Y. Sun, Y. Zhao, J. Wang, J. Liang, C. Wang, Q. Sun, X. Lin, K. R. Adair, J. Luo, D. Wang, R. Li, M. Cai, T. K. Sham, X. Sun, *Adv. Mater.* **2019**, *31*, 1806541.
- [11] a) Y. Yang, J. Xiong, S. Lai, R. Zhou, M. Zhao, H. Geng, Y. Zhang, Y. Fang, C. Li, J. Zhao, *ACS Appl. Mater. Interfaces* **2019**, *11*, 6118–6125; b) Y. Shuai, Z. Zhang, K. Chen, J. Lou, Y. Wang, *Chem. Commun.* **2019**, *55*, 2376–2379; c) H. Zhang, G. G. Eshetu, X. Judez, C. Li, L. M. Rodriguez-Martinez, M. Armand, *Angew. Chem. Int. Ed.* **2018**, *57*, 15002–15027.
- [12] K. R. Adair, C. Zhao, M. N. Banis, Y. Zhao, R. Li, M. Cai, X. Sun, *Angew. Chem.* **2019**, *131*, 15944–15949.
- [13] Y. X. Yao, X. Q. Zhang, B. Q. Li, C. Yan, P. Y. Chen, J. Q. Huang, Q. Zhang, *InfoMat* **2020**, *2*, 379–388.
- [14] a) L. Wang, Q. Wang, W. Jia, S. Chen, P. Gao, J. Li, *J. Power Sources* **2017**, *342*, 175–182; b) J. Liang, X. Li, Y. Zhao, L. V. Goncharova, G. Wang, K. R. Adair, C. Wang, R. Li, Y. Zhu, Y. Qian, L. Zhang, R. Yang, S. Lu, X. Sun, *Adv. Mater.* **2018**, *30*, 1804684.
- [15] Q. Pang, L. Zhou, L. F. Nazar, *Proc. Natl. Acad. Sci. USA* **2018**, *115*, 12389–12394.
- [16] a) A. A. Assegie, J. H. Cheng, L. M. Kuo, W. N. Su, B. J. Hwang, *Nanoscale* **2018**, *10*, 6125–6138; b) J. Luo, C.-C. Fang, N.-L. Wu, *Adv. Energy Mater.* **2018**, *8*, 1701482.
- [17] L. Wang, L. Zhang, Q. Wang, W. Li, B. Wu, W. Jia, Y. Wang, J. Li, H. Li, *Energy Storage Mater.* **2018**, *10*, 16–23.
- [18] E. Cha, M. D. Patel, J. Park, J. Hwang, V. Prasad, K. Cho, W. Choi, *Nat. Nanotechnol.* **2018**, *13*, 337.
- [19] Y. Zhang, T. T. Zuo, J. Popovic, K. Lim, Y. X. Yin, J. Maier, Y. G. Guo, *Mater. Today* **2020**, *33*, 56–74.
- [20] X. Liang, Q. Pang, I. R. Kochetkov, M. S. Sempere, H. Huang, X. Q. Sun, L. F. Nazar, *Nat. Energy* **2017**, *2*, 17119.
- [21] a) B. Sun, J. Lang, K. Liu, N. Hussain, M. Fang, H. Wu, *Chem. Commun.* **2019**, *55*, 1592–1595; b) W. Tang, X. Yin, S. Kang, Z. Chen, B. Tian, S. L. Teo, X. Wang, X. Chi, K. P. Loh, H. W. Lee, G. W. Zheng, *Adv. Mater.* **2018**, *30*, 1801745; c) Z. Tu, S. Choudhury, M. J. Zachman, S. Wei, K. Zhang, L. F. Kourkoutis, L. A. Archer, *Nat. Energy* **2018**, *3*, 310; d) S. Qu, W. Jia, Y. Wang, C. Li, Z. Yao, K. Li, Y. Liu, W. Zou, F. Zhou, Z. Wang, *Electrochim. Acta* **2019**, *317*, 120–127.
- [22] a) S. Choudhury, Z. Tu, S. Stalin, D. Vu, K. Fawole, D. Gunceler, R. Sundararaman, L. A. Archer, *Angew. Chem. Int. Ed.* **2017**, *56*, 13070–13077; *Angew. Chem.* **2017**, *129*, 13250–13257; b) F. Chu, J. Hu, J. Tian, X. Zhou, Z. Li, C. Li, *ACS Appl. Mater. Interfaces* **2018**, *10*, 12678–12689; c) N. S. Ergang, J. C. Lytle, K. T. Lee, S. M. Oh, W. H. Smyrl, A. Stein, *Adv. Mater.* **2006**, *18*, 1750.
- [23] M. Ma, Y. Lu, Z. Yan, J. Chen, *Batteries* **2019**, *2*, 663–667.
- [24] B. Sun, J. L. Lang, K. Liu, N. Hussain, M. H. Fang, H. Wu, *Chem. Commun.* **2019**, *55*, 1592–1595.
- [25] H. Zhong, Y. X. Wu, F. Ding, L. Sang, Y. H. Mai, *Electrochim. Acta* **2019**, *304*, 255–262.
- [26] C. L. Wang, S. J. Qu, J. Z. Li, *Energy Storage Mater.* **2020**, *9*, 368–374.
- [27] N. Kumagai, Y. Kikuchi, K. Tanno, F. Lantelme, M. Chemla, *J. Appl. Electrochem.* **1992**, *22*, 728–732.
- [28] a) Z. Shi, M. L. Liu, J. L. Gole, *Proteomics* **2000**, *3*, 312–315; b) R. A. Huggins, *J. Power Sources* **1988**, *22*, 341–350.
- [29] A. Varzi, L. Mattarozzi, S. Cattarin, P. Guerriero, S. Passerini, *Adv. Energy Mater.* **2018**, *8*, 1701706.
- [30] P. Shi, X. Q. Zhang, X. Shen, R. Zhang, H. Liu, Q. Zhang, *Adv. Mater.* **2020**, *5*, 1900806.
- [31] a) L. Y. Qi, Z. W. Wu, B. L. Zhao, B. J. Liu, W. Y. Wang, H. Pei, Y. Q. Dong, S. J. Zhang, Z. J. Yang, L. L. Qu, W. Zhang, *Chem. Eur. J.* **2020**, *26*, 4193–4203; b) F. Croce, G. B. Appetecchi, L. Persi, B. Scrosati, *Nature* **1998**, *394*, 456–458.

Manuscript received: June 1, 2020

Revised manuscript received: July 28, 2020

Accepted manuscript online: August 19, 2020

Version of record online: September 22, 2020